Accepted Manuscript

Simulation of hypersonic flows with equilibrium chemical reactions on graphics processor units

V. Emelyanov, A. Karpenko, K. Volkov

Simulation of hypersonic flows with equilibrium chemical reactions on graphics processor units

V. Emelyanov[1], A. Karpenko[2, *], K. Volkov[3]

[1]Baltic State Technical University, St Petersburg, 190005, Russia

[2]Saint Petersburg State University, St Petersburg, 198504, Russia

[3]Kingston University, London, SW15 3DW, United Kingdom

Abstract

When hypersonic vehicle travels in the atmosphere with a high speed, the surrounding gas experiences complicated physical and chemical processes producing high-temperature gas effects. High-temperature gas effects are a key issue related to hypersonic aerodynamic design and optimization. The finite volume method is applied to solve unsteady three-dimensional compressible Navier–Stokes equations on unstructured meshes. High-temperature gas effects altering the aerodynamics of vehicle are taken into account. Possibilities of the use of graphics processor units (GPUs) for the simulation of hypersonic flows are demonstrated. Solutions of some benchmark test cases on GPUs are reported, and a comparison between computational results of chemically equilibrium reacting and perfect air flowfields is performed. Speedup of solution of the problems of interest on GPUs with respect to their solution on central processor units (CPUs) is compared. The results obtained provide promising perspective for designing a GPU-based software framework for applications in CFD.

Keywords

Flight safety; Hypersonic flow; High-temperature air; Unstructured mesh; Graphics processor unit; Parallel algorithm

1 Introduction

Development and implementation of methods and tools that adequately model fundamental physics and allow credible physics-based optimization for future operational hypersonic vehicle systems are becoming more important due to requirements of ensuring their flight safety [1,2]. The aero-thermodynamic design and optimization of hypersonic vehicles includes wind tunnel testing, flight experiments and computer simulation [3]. Many aerodynamic and propulsion characteristics still remain uncertain and are difficult to predict due to the lack of flight test data and limitations of ground test facilities [4–6]. The ground-based experimental facilities are not able to reproduce full-scale complex physical and chemical phenomena conditions for flight due to short duration of useful test times [7, 8].

The methods of computational fluid dynamics (CFD) are extensively applied in design and optimization of hypersonic vehicles to get more insight into complex flowfields. Computer simulation is particularly attractive due to its relatively low cost and its ability to deliver data that cannot be measured or observed. Specific challenges involved in modelling and control of hypersonic vehicles, the current state of research and some future directions

---

*Corresponding author: aspera.2003.ru@mail.ru

are described in [9–11]. Flow discontinuities, high gradients of flow quantities, turbulence effects, flow separation and other flow features impose great demands on the underlying numerical methods. The quality of CFD calculations of hypersonic flows strongly depends on the proper prediction of flow physics (non-equilibrium effects, radiation, molecular dissociation, chemical reactions). Investigations of heat transfer, skin friction, secondary flows, flow separation and re-attachment effects demand reliable numerical methods, accurate programming and robust working practices.

At hypersonic speeds, the aero-thermodynamic properties of the air deviate from the perfect gas behavior. High-temperature gas effects alter the aerodynamics of vehicles as their behavior is significantly different to that of a perfect gas. When a vehicle travels through the atmosphere at hypersonic speed, the Mach number is high and the bow shock wave is strong. The temperatures behind the normal shock wave increase with the Mach number. After the air crosses the shock, its enthalpy is sufficient to cause dissociation of air molecules and to induce chemical reactions behind the shock wave [12]. The boundary layer around the vehicle becomes thicker due to high-temperature gas effects of hypersonic flow regime. Thick boundary layer, flow separation and reattachment phenomena lead to viscous behavior in terms of pressure distribution, shock waves and drag, differing significantly from the results of the inviscid flow characteristics [9].

Increasing air temperature above a certain threshold, molecular vibrational mode starts becoming important [3]. The vibrational energy of the molecules becomes excited, and this causes the specific heat capacities to become functions of temperature. Further increase the air temperature leads to molecular dissociation and recombination reactions. As the gas temperature is further increases, chemical reactions occur. For a chemically equilibrium reacting gas specific heat capacities are functions of both temperature and pressure. For higher temperatures, the process of atomic ionization takes place [13]. These processes have a significant impact on the properties of the air. The air can no longer be treated as a perfect gas. For example, at a pressure of 1 atm, oxygen and nitrogen vibrational excitation becomes important above a temperature 800 K. Oxygen dissociation ($O_2 \rightarrow 2O$) begins at about 2000 K, and the molecular oxygen is essentially totally dissociated at 4000 K. At this temperature nitrogen dissociation ($N_2 \rightarrow 2N$) begins, and is totally dissociated at 9000 K. Above a temperature of 9000 K, ions are formed ($O \rightarrow O^+ + e^-$, $N \rightarrow N^+ + e^-$), and the gas becomes a partially ionized plasma. At temperature higher 9000 K, all the nitrogen and oxygen molecules have already dissociated and atomic ionization starts taking place [3].

High-temperature gas effects are a key issue related to hypersonic aerodynamic design and are currently poorly to moderately modelled in CFD [15]. Thin shock layers due to high compression, entropy layers caused by highly swept and curved shock waves, viscous/inviscid interactions and real gas effects are all complex flow features that occur in hypersonic flow [3]. There is also restriction in the speed of computers and a limitation of reliable quantitative data about high-temperature constants [13]. Extensive calculations of the equilibrium properties of high-temperature air, including the equilibrium composition, are presented in [14].

A number of studies have tried to quantify high-temperature gas effects in shock/shock interaction regions using detailed numerical solutions. Significant efforts have focused on simple axisymmetric geometries that are chosen to highlight the important flow field physics in a two-dimensional environment without three-dimensional effects [16–18]. The readiness of CFD to simulate high-enthalpy flows is assessed in [19]. The carbuncle problem represents a local unpleasant displacement of the bow shock wave shape, which strongly affects heat transfer to the vehicle [20]. The analysis of various methods and finite-difference schemes for numerical simulation of reactive flows is performed in [21,22]. The use of gradient information for the acceleration of uncertainty quantification within the context of viscous hypersonic

flows is examined in [23]. Results of simulation of high-enthalpy flows with a Mach number range between 6.4 and 25.9 are provided in [24].

Although a large number of non-equilibrium simulation codes have been developed [25, 26], the implementation of the numerical solvers is not considered as fully completed because of limited information with regard to physical model (chemical reactions, transport models) and also validation (lack of both numerical solutions and experimental results for comparison). These methods require extensive computer processor time and storage, and are not generally applicable to parametric and optimization studies or preliminary design calculations. The complex physical phenomena and a wide range of spatial and time scales present in hypersonic flows making the development of efficient and accurate numerical simulation methods challenging.

Speed and accuracy are key factors in the evaluation of CFD solver performance. High performance computing (HPC) resources are widely used in aerospace applications. However, the stagnation in the clock-speed of central processing units (CPUs) has led to significant interest in parallel architectures that offer increasing computational power by using many separate processing units. Modern graphics processing units (GPUs) provide new programming models that enable to harness their large processing power and to design CFD simulations at both high performance and low cost. The use of GPUs is a cost effective way of improving substantially the performance in CFD applications [27]. GPU platforms make it possible to achieve speedups of an order of magnitude over a standard CPU in many CFD applications. The motivation of this study is to assess the in-house compressible CFD code for hypersonic flow simulations and to demonstrate successful design of a highly parallel computation system based on GPUs. Possibilities of the use of GPUs for the simulation of high-speed and high-temperature flows are discussed. The results obtained are generally in a reasonable agreement with the available experimental and computational data, although some important sensitivities are identified.

2   Governing equations

Mathematical model used for numerical simulation of hypersonic flows with high-temperature gas effects has to capture the complex thermo-physical phenomena that characterize these flows.

2.1   Gas dynamics

The unsteady three-dimensional flow of the viscous compressible gas is described with a system of equations including mass conservation equation, momentum conservation equation and energy conservation equation. Integration over control volume V allows to present governing equations in the integral form

$$\frac{\partial}{\partial t} \oint_V \boldsymbol{U} dV + \oint_{\partial V} \boldsymbol{F} \cdot d\boldsymbol{S} = 0, \tag{1}$$

where $\boldsymbol{U}$ is the vector of conservative variables in point $\boldsymbol{x}$ at time t, $\boldsymbol{F}$ is the flux tensor with dimension 3×5, $d\boldsymbol{S} = \boldsymbol{n} dS$ is the surface area vector, $\boldsymbol{n}$ is the surface normal vector. The vector of conservative variables and flux tensor are presented in the form

$$\boldsymbol{U} = \begin{pmatrix} \rho \\ \rho \boldsymbol{v} \\ \rho e \end{pmatrix}, \quad \boldsymbol{F} = \begin{pmatrix} \rho \boldsymbol{v} \\ \rho \boldsymbol{v}^* \otimes \boldsymbol{v} + p\boldsymbol{I} - \boldsymbol{\tau} \\ (\rho e + p)\boldsymbol{v} - \boldsymbol{v} \cdot \boldsymbol{\tau} + \boldsymbol{q} \end{pmatrix}.$$

The viscous terms in the governing equations (viscous stresses and heat fluxes) require constitutive relations to relate these viscous terms to the flow and thermodynamic variables. The components of the viscous stress tensor have the form

$$\tau_{ij} = \mu \left(\frac{\partial v_i}{\partial x_j} + \frac{\partial v_j}{\partial x_i} - \frac{2}{3} \frac{\partial v_k}{\partial x_k} \delta_{ij} \right).$$

The heat flux vector is found from the Fourier law

$$\boldsymbol{q} = -\lambda \nabla T,$$

Here, t is the time, ρ is the density, p is the pressure, T is the temperature, $\boldsymbol{v}$ is the velocity vector with components v_x, v_y and v_z in cartesian directions x, y and z, e is the total energy per unit mass, $\boldsymbol{q}$ is the heat flux, $\boldsymbol{\tau}$ is the viscous stress tensor, $\boldsymbol{I}$ is the identity tensor. Star denotes the conjugate tensor.

The equation of state of a perfect gas has the form

$$p = \rho \frac{R_0}{M(p,T)} T,$$

where R_0 is the universal gas constant, M is the molecular weight of the mixture, which depends on the pressure and temperature.

The total energy is equal to the sum of the internal energy (it includes the energies of translational, rotational, vibrational motions and electronic excitation of atomic and molecular components of the gas mixture) and kinetic energy

$$e = \varepsilon + \frac{1}{2} |\boldsymbol{v}|^2,$$

where ε is the specific internal energy. It is assumed that there is equilibrium over all internal degrees of freedom of particles with an energy of translational motion. Using the enthalpy $h = \varepsilon + p/\rho$, the expression for the total energy is written as

$$e = h + \frac{1}{2} |\boldsymbol{v}|^2 - \frac{p}{\rho}.$$

Specific enthalpy of the gas is

$$h = h_0 + \int_{T_0}^{T} c_p dT,$$

where h_0 is the enthalpy at the reference temperature T_0. For a perfect gas, the molecular weight and the gas constant ($R = R_0/M$), the specific heat capacities at constant pressure and constant volume are constant and the Mayer's relationship takes place ($c_p - c_v = R$).

The Sutherland's law is used to obtain molecular viscosity as a function of temperature

$$\frac{\mu}{\mu_*} = \left(\frac{T}{T_*} \right)^{3/2} \frac{T_* + S_0}{T + S_0},$$

where $\mu_* = 1.68 \times 10^{-5}$ kg/(m·s) is the viscosity at the reference temperature $T_* = 273$ K, and $S_0 = 110.5$ K for air. Sutherland's law is accurate for air over a range of several thousand degrees and is appropriate for hypersonic viscous flow calculations. The thermal conductivity is obtained from dynamic viscosity and the Prandtl number, $\lambda = c_p \mu / \text{Pr}$. For air at standard conditions, $\text{Pr} = 0.71$.

2.2 Chemical reactions

The chemical equilibrium assumption consists of considering that all the species in the system have enough time to reach the equilibrium state. In general, if the mixture has N_s species and N_e elements, then $N_s - N_e$ independent chemical equations with the appropriate equilibrium constants are considered. The remaining equations are obtained from the mass balance equation and Dalton's law of partial pressures.

In numerical calculations, air is represented as a mixture of $N_s = 11$ different ideal gases (e^-, N, O, Ar, N_2, O_2, NO, N^+, O^+, Ar^+, NO^+). The distribution of chemical elements is given by the molar fraction $\chi_i^0 = \nu_i^0 / \nu_\Sigma^0$, where $\nu_\Sigma^0 = \sum_i^{N_e} \nu_i^0$, and ν_i^0 is the number of moles of the chemical element i. The superscript 0 indicates that the number of moles is considered for the chemical element, and not for the molecule or component of the mixture. The partial pressure of an ideal gas in a mixture equals the pressure that is a gas if it occupies the same volume as the entire gas mixture at the same temperature. The partial pressure of the gas mixture component k is related to the mole fractions by the relation $\chi_k = \nu_k / \nu_\Sigma = p_k / p_\Sigma$, where p_Σ is the pressure of the mixture. To simplify the formulation of the equilibrium equations, it is assumed that upon dissociation of any molecule, its dissociation occurs up to the atoms of the elements. Therefore, the number of reactions is equal to the difference of accounted components of the mixture N_s and the number of considered chemical elements N_e ($N_l = N_s - N_e$, where $l = 1, \ldots, N_l$).

The system of equations describing the equilibrium composition of the mixture includes the following equations

$$
\begin{aligned}
&\sum_k^{N_s} \phi_i^k \chi_k = \chi_i^0 \frac{\nu_\Sigma^0}{\nu_\Sigma} \quad (i = 1, \ldots, N_e); \\
&p_\Sigma^{\beta^l} \prod_k^{N_s} \chi_k^{\eta_k^l} = K_p^l, \quad \beta^l = \sum_k^{N_s} \eta_k^l \quad (l = 1, \ldots, N_l); \\
&\sum_k^{N_s} \chi_k = 1.
\end{aligned}
\tag{2}
$$

Here, ϕ_i^k is the number of particles of the chemical element i in the mixture component k, $\chi_k = \nu_k / \nu_\Sigma$ is the molar fraction of gas mixture components, ν_k is the number of moles of the component of the mixture, $\nu_\Sigma = \sum_k^{N_s} \nu_k$ is the total number of moles of the gas mixture in the current state, K_p^l is the constant of chemical equilibrium with respect to pressure (subscript p) of the reaction l, η_k^l are the stoichiometric coefficients for the reaction l, which are negative for the initial products and positive for the reaction products. In the system (2), there are $N_s + 1$ equations with unknowns $\nu_\Sigma^0 / \nu_\Sigma$ and $\chi_1, \chi_2, \ldots, \chi_{N_s}$.

The equilibrium constant K_p^l is related to the Gibbs energy for products participating in this reaction by the relation

$$
RT \ln K_p^l = -\sum_k^{N_s} \eta_k^l \Delta G_k.
$$

The change in the Gibbs energy of the component of the mixture k from the standard state to the state at the given temperature, ΔG_k, is expressed as

$$
\Delta G_k(T) = \Delta H_k(T) - T \Delta S_k(T),
$$

where $\Delta H_k(T)$ is the change in molar enthalpy from the standard state, $\Delta S_k(T)$ is the change in entropy. The functions $\Delta H_k(T)$ and $\Delta S_k(T)$ for each component of the mixture

k are calculated using polynomial approximations. The equilibrium constant is found from the equation

$$R \ln K_p^l = \sum_k^{N_s} \eta_k^l \Delta\Phi_k(T) - \frac{1}{T} \sum_k^{N_s} \eta_k^l \Delta H_k(0).$$

The change in the Gibbs energy, $\Delta G_k(T)$, is expressed in terms of the reduced Gibbs function, $\Delta\Phi_k(T)$, and the formation enthalpy, $\Delta H_k(0)$.

2.3   High-temperature effects

In the chemically equilibrium reacting flows, the chemical components computation is time consuming. The explicit expressions derived in [30] for equilibrium air are based on density and internal energy as the independent variables. These expressions are used to determine the other thermodynamic and transport properties, avoiding calculating chemical species. When high-temperature effects are taken into account, the system of equations (2) is not solved, and explicit expressions for the molecular weight and enthalpy as functions of pressure and temperature, $M_\Sigma = M_\Sigma(p, T)$ and $h = h(p, T)$, proposed in [30], are applied to simplify calculations. Other models dealing with real gas effects (for example, Lighthill model) are also available in the literature. However, these models were not validated for a wide range of conditions.

The model proposed in [30] takes into account the dissociation of oxygen and nitrogen, formation of nitric oxide, possibility of the appearance of an electronic component due to the single and double ionization of oxygen, nitrogen and argon. The oxygen dissociation reaction takes place, followed by reactions of nitrogen dissociation and single ionization of a weighted average mixture of these gases. When considering each subsequent reaction, the previous one is considered as fully completed. In the temperature range from 200 to 20000 K and pressures from 0.001 to 1000 atm, the error of the model does not exceed 1.5% by density and 3% by enthalpy.

To extend the existing numerical methods developed for a perfect gas to hypersonic flows with high-temperature effects, an effective ratio of specific heat capacities is introduced. It makes it possible to calculate the speed of sound from the relation

$$a^2 = \gamma_* \frac{p}{\rho}.$$

The relation between the effective ratio of specific heat capacities, γ^*, and the ratio of specific heat capacities of perfect gas, $\gamma = c_p/c_v$, is

$$\gamma_* = \gamma \frac{\rho}{p\rho_p}.$$

For isentropic conditions ($ds = 0$), the speed of sound is calculated as

$$a^2 = \left(\frac{\partial p}{\partial \rho}\right)_s = \left(\rho_p + \rho_T \frac{dT}{dp}\right)^{-1}.$$

In thermodynamic equilibrium, the relation $T ds = dh - dp/\rho$ is valid. Since $dh = h_p dp + h_T dT$, then

$$\frac{dT}{dp} = \frac{1 - \rho h_p}{\rho h_T}.$$

The specific heat capacity at constant pressure is calculated using central finite differences of the second order

$$c_p(p, T) = \left(\frac{\partial h}{\partial T} \right)_p = \frac{h(p, T + \Delta T) - h(p, T - \Delta T)}{2\Delta T},$$

where $\Delta T = 0.01T$.

For shock wave calculations, the effective adiabatic index is defined as $\gamma_s = h/\varepsilon$, and the specific internal energy is found from the relation $\varepsilon = p/[(\gamma_s - 1)\rho]$. The effective ratio of specific heat capacities is defined as

$$\gamma_e = \frac{c_p}{c_v} \left[1 + \frac{p}{M} \left(\frac{\partial M}{\partial p} \right)_T \right]^{-1},$$

where M is the molar mass.

3   Computational procedure

The governing equations are solved with in-house finite volume code run on unstructured meshes consisting of cells of various topology.

3.1   Numerical method

The non-linear solver works in an explicit time-marching fashion, based on a Runge–Kutta stepping procedure. The unstructured CFD code uses an edge-based data structure to give the flexibility to run on meshes composed of a variety of cell types. The fluxes through the surface of a cell are calculated on the basis of flow variables at nodes at either end of an edge, and an area associated with that edge (edge weight). The edge weights are pre-computed and take into account geometry of the cell. The flux vector is split into the inviscid and viscous components. The governing equations are solved with upwind finite difference scheme for inviscid fluxes, and central difference scheme of the second order for viscous fluxes.

The governing equation (1) is written in the form

$$\frac{d\boldsymbol{U}_i^n}{dt} + \boldsymbol{L}(\boldsymbol{U}_i^n) = 0, \tag{3}$$

where $\boldsymbol{L}(\boldsymbol{U}_i^n)$ is the spatial differential operator. The subscript i refers to the control volume, and the superscript n refers to the time layer. The flow variables vector averaged over the control volume V_i is

$$\boldsymbol{U}_i = \frac{1}{V_i} \int_{V_i} \boldsymbol{U} dV.$$

The flow residual within each cell of unstructured mesh is given by the sum of the normal inviscid and viscous fluxes over all faces

$$\boldsymbol{R}_i(\boldsymbol{U}) = -\frac{1}{V_i} \sum_j^{N_i} \boldsymbol{F}_{ij}(\boldsymbol{U}) S_{ij}, \tag{4}$$

where $\boldsymbol{F}_{ij}$ is the numerical flux from cell i through the face j at the face center, V_i is the volume of cell i, S_{ij} is the area of the face j of the cell i, N_i is the number of faces of the cell i.

The inviscid flux is calculated using gradient reconstruction of primitive variables. The calculations of gradients are based on Green–Gauss theorem. The inviscid flux is found from the relation

$$\boldsymbol{F}(\boldsymbol{U}_L, \boldsymbol{U}_R) = \frac{1}{2}\Big[\boldsymbol{F}(\boldsymbol{U}_L) + \boldsymbol{F}(\boldsymbol{U}_R) - |A|\,(\boldsymbol{U}_R - \boldsymbol{U}_L)\Big].$$

where the subscripts L and R refer to cells on the left and on the right edges of the control volume. The matrix A is presented in the form $A = R\Lambda L$, where Λ is the diagonal matrix composed from the Jacobian eigenvalues, and R and L are the matrices composed from its right and left eigenvectors, respectively. The flow variables are found as

$$\boldsymbol{U}'_L = \boldsymbol{U}_L + \varphi_L \nabla \boldsymbol{U}_L \cdot \Delta \boldsymbol{r}_L;$$
$$\boldsymbol{U}'_R = \boldsymbol{U}_R + \varphi_R \nabla \boldsymbol{U}_R \cdot \Delta \boldsymbol{r}_R.$$

Here, $\Delta \boldsymbol{r}_L$ and $\Delta \boldsymbol{r}_R$ are the distance vectors from the cell center to the face center, $\nabla \boldsymbol{U}_L$ and $\nabla \boldsymbol{U}_R$ are the gradients calculated in the cell center, φ_L and φ_R are the limiter functions in the cell. Gradients of flow variables are found from expression

$$(\nabla \boldsymbol{U})^l_i = \frac{1}{V_i} \sum_{k=1}^{N_i} \frac{1}{2}\,(\boldsymbol{U}_i + \boldsymbol{U}_k)\,n_l S_{ik},$$

where n_l is the component of normal vector. Wall boundary conditions are realized using ghost cells.

Rusanov scheme is also used to calculate numerical fluxes. The idea behind Rusanov scheme, instead of approximating the exact Riemann solver, is to recall that the entropy solution is the limit of viscous solutions and to take a centred flux to which some viscosity (with the right sign) is added. Rusanov scheme has good stability properties without needing to solve the Riemann problem.

3.2 Chemical kinetics

The calculation of a chemical equilibrium composition is conceptually straightforward. New variables $x_1 = \ln \chi_1$, $x_2 = \ln \chi_2$, ..., $x_{N_s} = \ln \chi_{N_s}$, $x_{N_s+1} = \nu^0_\Sigma / \nu_\Sigma$ are introduced to solve the system of equations (2). Taking the logarithm of the equations of chemical equilibrium gives

$$\sum_k^{N_s} \phi_i^k e^{x_k} - \chi_i^0 x_{N_s+1} = 0 \qquad (i = 1, \ldots, N_e);$$

$$\sum_k^{N_s} \eta_k^l x_k + \beta^l \ln p_\Sigma - \ln K_p^l = 0, \quad \beta^l = \sum_k^{N_s} \eta_k^l \qquad (l = 1, \ldots, N_l); \tag{5}$$

$$\sum_k^{N_s} e^{x_k} - 1 = 0.$$

The linearization of the equations (5) using Taylor series expansion leads to the equations

$$\sum_k^{N_s} \phi_i^k \chi_k \Delta x_k - \chi_i^0 \Delta x_{N_s+1} = -\left(\sum_k^{N_s} \phi_i^k \chi_k - \chi_i^0 x_{N_s+1}\right) \qquad (i=1,\ldots,N_e);$$

$$\sum_k^{N_s} \eta_k^l \Delta x_k = -\left(\sum_k^{N_s} \eta_k^l x_k + \beta^l \ln p_\Sigma - \ln K_p^l\right) \qquad (l=1,\ldots,N_l);$$

$$\sum_k^{N_s} \chi_k \Delta x_k = -\left(\sum_k^{N_s} \chi_k - 1\right).$$

The linearized system is written with respect to unknown increments in the matrix form

$$A\Delta \boldsymbol{x} = \boldsymbol{b},$$

where A is the matrix of coefficients, $\boldsymbol{b}$ is a vector of right-hand sides, and $\Delta \boldsymbol{x}$ is a change in the solution vector between the iterations. The solution at the iteration $n+1$ is found as

$$\boldsymbol{x}^{n+1} = \boldsymbol{x}^n + (1+\theta)\Delta \boldsymbol{x},$$

where θ is the coefficient of lower relaxation, which is used to ensure the stability of the numerical procedure.

To solve the system of equations (2), it is necessary to set the total pressure of the mixture p_Σ and the temperature T. The chemical composition of the reacting mixture is expressed in terms of mole fractions, χ_k. The molecular weight and specific enthalpy of the mixture are found from the relationships

$$M_\Sigma = \sum_k^{N_s} M_k \chi_k, \quad h = \frac{1}{M_\Sigma} \sum_k^{N_s} H_k \chi_k,$$

where M_k is the molecular weight of the mixture component k.

3.3 Parallel algorithm

The computational procedure is implemented as a computer code in C/C++ programming language. Parallelization of the computational procedure is performed by a message passing interface (MPI). CUDA technology is used to implement GPU version of the solver [27]. An equivalent solver is made in C++ to be run on CPU for benchmarking purposes. Each time step of the computation involves a series of kernels on the GPU which evaluate the cell face fluxes, sum the fluxes into the cell, calculate the change in properties at each node, smooth the variables and apply boundary conditions.

To compare the performance of the CFD solver on CPU and GPU, similar algorithms for calculating the perfect gas and equilibrium air are implemented on CPU. Calculations are made on two different servers. Server 1 uses one core of the Xeon E5-2680 v3 CPU or one NVidia Tesla K40 calculation module. Server 2 uses one IBM Power8 CPU thread or one NVidia Tesla K40 module. Some characteristics of the servers used in CFD calculations are presented in the Table 1.

Table 1. Parameters of GPU harware

Server	Server 1		Server 2	
Brand name	Huawei RH2288H		IBM S822LC	
RAM per node, GB	128		256	
Number of CPUs	2		2	
Number of GPUs	2		2	
Processor unit	Xeon E5-2680 v3	Tesla K40	IBM Power8	Tesla P100
Production year	2014	2013	2016	2016
Frequency (base), MHz	2500	745	2860	1328
Number of cores	12	2880	10	3584
Peak performance, GFlops (single precision, base)	960	4291	458 458	9519
Peak performance, GFlops (double precision, base)	480	1430	229	4760
Memory bus width, bit	64	384	64	4096
RAM per socket, Gb	768	12	512	16
Bandwidth of memory bus per socket, Gb/s	68	288	115.2	732

4   Composition of air

The numerical calculations are carried out for the model of air consisting of 11 species (e^-, N, O, Ar, N_2, O_2, NO, N^+, O^+, Ar^+, NO^+). The air represents the mixture of 78% N_2, 21% O_2 and 1% Ar.

Composition of high-temperature air is shown in the Figure 1 and Figure 2 where the equilibrium composition of high-temperature air (in terms of mole fraction) is given as a function of temperature at $p = 0.01$ atm. The oxygen begins to dissociate above 2100 K and is completely dissociated above 7800 K. The nitrogen begins to dissociate above 6000 K and is completely dissociated above 12000 K. The NO is present between 800 and 11000 K, with a peak mole fraction occurring about 2500 K. The line for O has a local maximum around 4000 K and then decreases at higher temperatures in the range from 6000 to 20000 K. This does not mean, however, that the total amount of O atoms is decreasing in this range. Rather, it is a consequence of the definition of mole fraction. Because $O = \sum O / \sum$, where $\sum O$ is the number moles of O and $\sum$ is the total number of moles, then O decreases simply because the total number of moles of the mixture is increasing (as a result of the dissociation of N_2, for example). The data plotted are in a good agreement with the detailed tabulations found in [14].

If the pressure is increased to 10 atm then all of the lines would qualitatively shift to the right, that is, the various dissociation processes would be delayed to higher temperatures. On the other hand, if pressure is decreased, then all of the lines would qualitatively shift to the left, that is, dissociation would occur at lower temperature. Hence, raising the pressure decreases the amount of dissociation, and lowering the pressure increases the amount of dissociation.

The equilibrium speed of sound is a function of both pressure and temperature, unlike the case for a calorically or thermally perfect gas where it depends on temperature only [3]. This is emphasized in the Figure 3 (effective specific heat capacity ratios, $\gamma_c = c_p/c_v$, γ_s and γ_e are shown), which gives the equilibrium speed of sound for high-temperature air as a function of both pressure and temperature. The difference between the frozen and equilibrium speeds
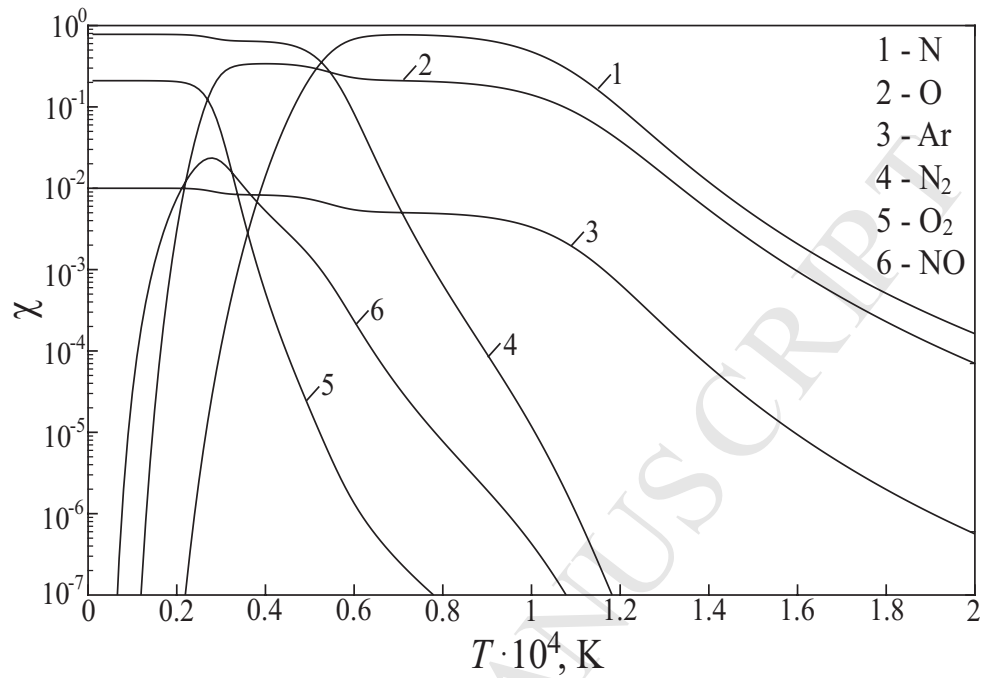
Figure 1. Composition of equilibrium air as a function of temperature at pressure 0.01 atm ($1 — N$, $2 — O$, $3 — Ar$, $4 — N_2$, $5 — O_2$, $6 — NO$)
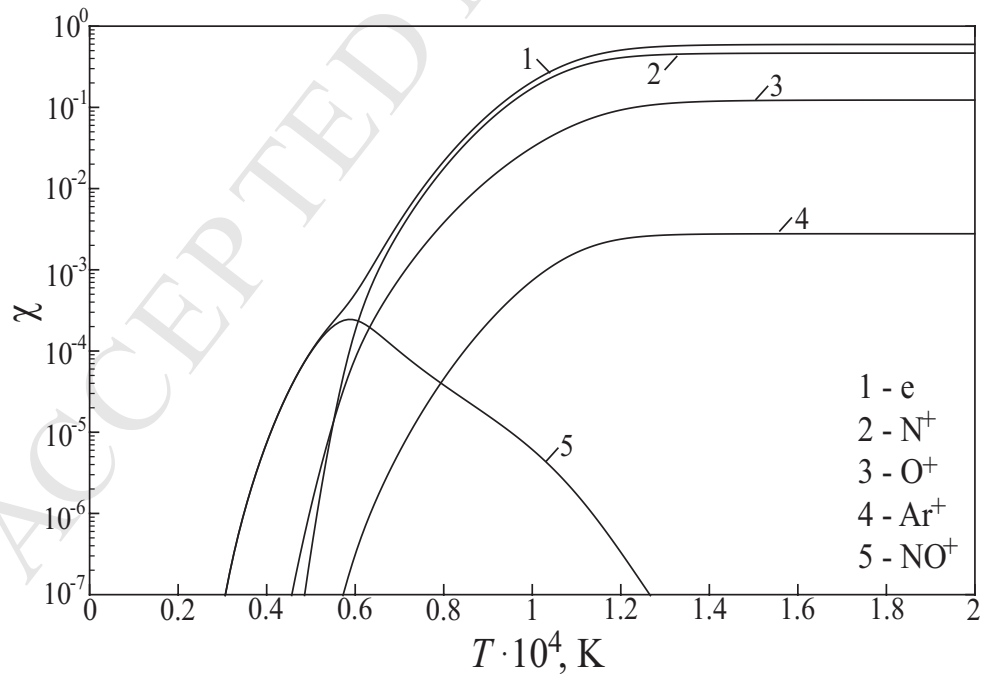

Figure 2. Composition of equilibrium air as a function of temperature at pressure 0.01 atm ($1 — e$, $2 — N^+$, $3 — O^+$, $4 — Ar^+$, $5 — NO^+$)

of sound in air can be as large as 20% under practical conditions. In turn, this once again underscores the ambiguity in the definition of Mach number for high-temperature flows.
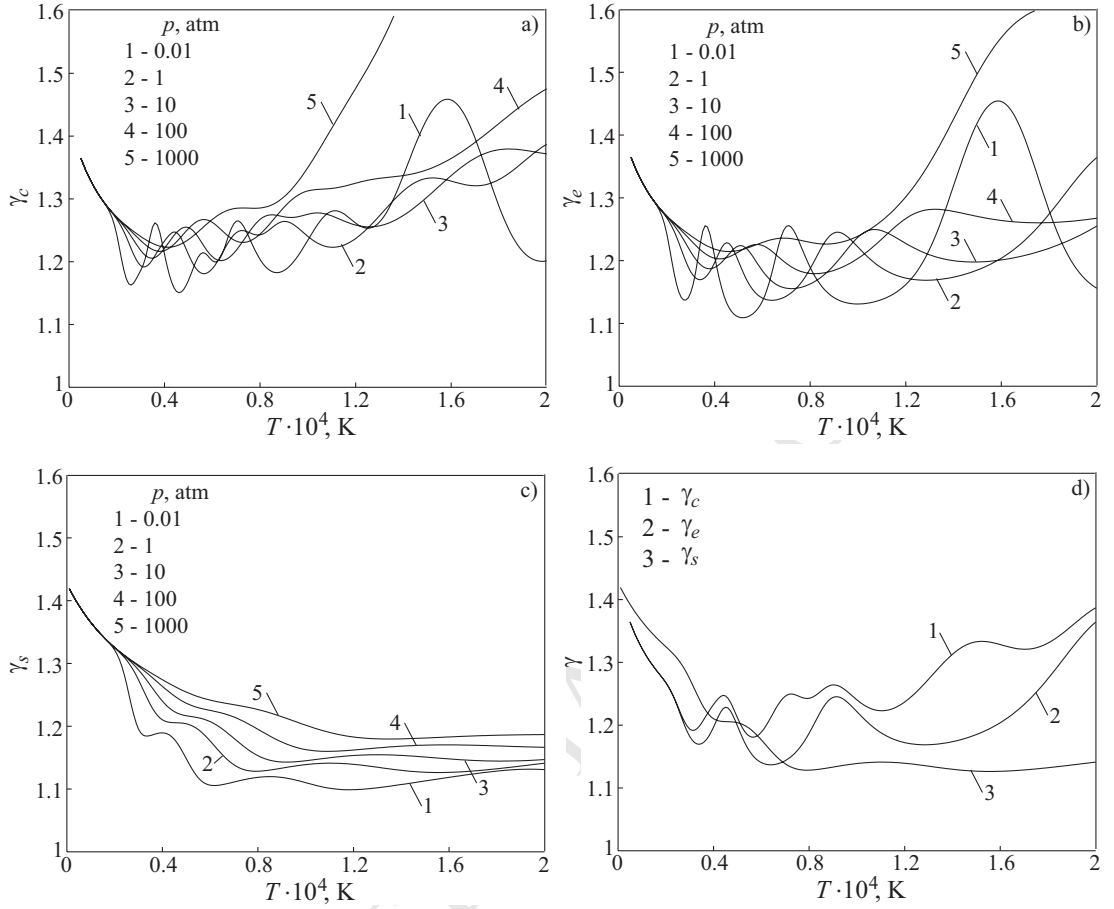
Figure 3. The effective ratios of specific heat capacities for air as functions of pressure and temperature (a, b and c) and the effective ratios of specific heat capacities for air as functions of temperature at the fixed pressure ($p = 1$ atm)

5   Results and discussion

The GPU version of the CFD code is validated for a variety of benchmark test cases. The benchmark problems provide insight into the ability of CFD solver and numerical schemes to capture the bow shock, smoothly resolve the post-shock stagnation region flow and predict a smoothly varying heating distribution around the stagnation point.

5.1   Hypersonic flow around sphere

Accurate simulation of stagnation region heating in hypersonic flows is a key requirement for acceptance of any algorithm proposed for use in aero-thermodynamic analysis. The shock standoff distance on sphere in hypersonic flow is one of the most appropriate parameter for validation of CFD results. For a high Mach number, the shock standoff distance is much smaller than the sphere radius. Its experimental measurement is difficult, and large errors have to be accepted. Some significant theoretical studies have been performed to predict the shock standoff distance on spheres in hypersonic flows [31, 32]. A theoretical model to find the shock standoff distance on axisymmetric blunt bodies for frozen and equilibrium flows is developed in [33]. The shock standoff distance becomes larger as the flow condition is changed from equilibrium to calorically perfect gas case [3]. The measured drag coefficients for spheres covering subsonic, supersonic and hypersonic regimes are given in [34].

The flow past a sphere with a diameter $D = 12.7$ mm in a hypersonic air flow with

equilibrium chemical reactions is considered. The flow parameters correspond to those used in experiments [31]. The inlet flow pressure is $p = 666.61$ Pa, and the inlet temperature is $T = 293$ K (the density is $\rho = 7.9 \times 10^{-3}$ kg/m^3). The Mach number varies in the range M = 7.1–17.77, which corresponds to the flight speed $V = 2438.4$–6705.6 m/s.

The computational domain is shown in the Figure 4. The distance between outer boundary of the computational domain and stagnation point is 4 mm, and the distance between outer boundary of the computational domain and top sphere point is 8.65 mm. The problem is solved on the mesh containing 1.6×10^5 cells. The supersonic inlet boundary conditions are specified on the inlet boundary, and supersonic outflow boundary conditions are specified on the outlet boundary. Slip and adiabatic boundary conditions are applied to the sphere surface.
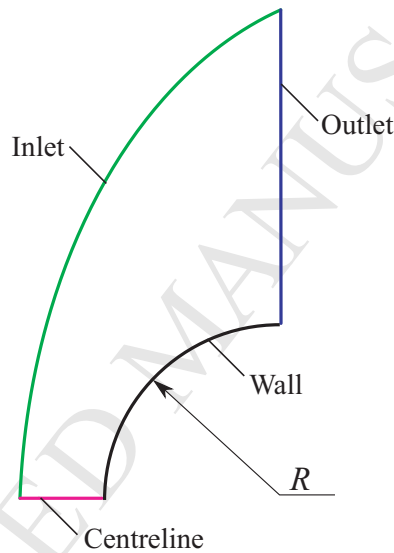
Figure 4. Computational domain and
boundary conditions

When the freestream Mach number is sufficiently high, the non-dimensional flow quantities become essentially independent of Mach number. Some typical results are shown in the Figure 5 for the fixed Mach number. Comparison of the results computed from the equilibrium chemically reacting case with similar results obtained from a calorically perfect gas with $\gamma = 1.4$ given in [3] for flow over a sphere show that the chemically reacting case exhibits higher densities and a thinner shock layer. Pressure reaches a maximum at the stagnation point and then decreases downstream. The high temperature effects on the flow variables become more pronounced with increasing free stream velocity, although the pressure is the least affected. The most intense dissociation occurs near the stagnation region, but the primary concentrations of nitrogen monoxide occur further downstream beyond the sonic line. Near the shock the mass fraction of oxygen is 0.22 and due to the high temperatures it dissociates and reacts with other air molecules as the flow moves downstream. Near the wall oxygen is almost completely dissociated but there is not a large amount of atomic oxygen.

The results have a reasonable agreement with experimental measurements. As Mach numbers increase, the entropy change across the shock also increases, which results in a strong entropy gradient and highly vortical flow that mixes with the boundary layer. High temperatures due to a manifestation of viscous dissipation cause non-equilibrium chemical flow properties such as vibrational excitation and dissociation and ionization of molecules
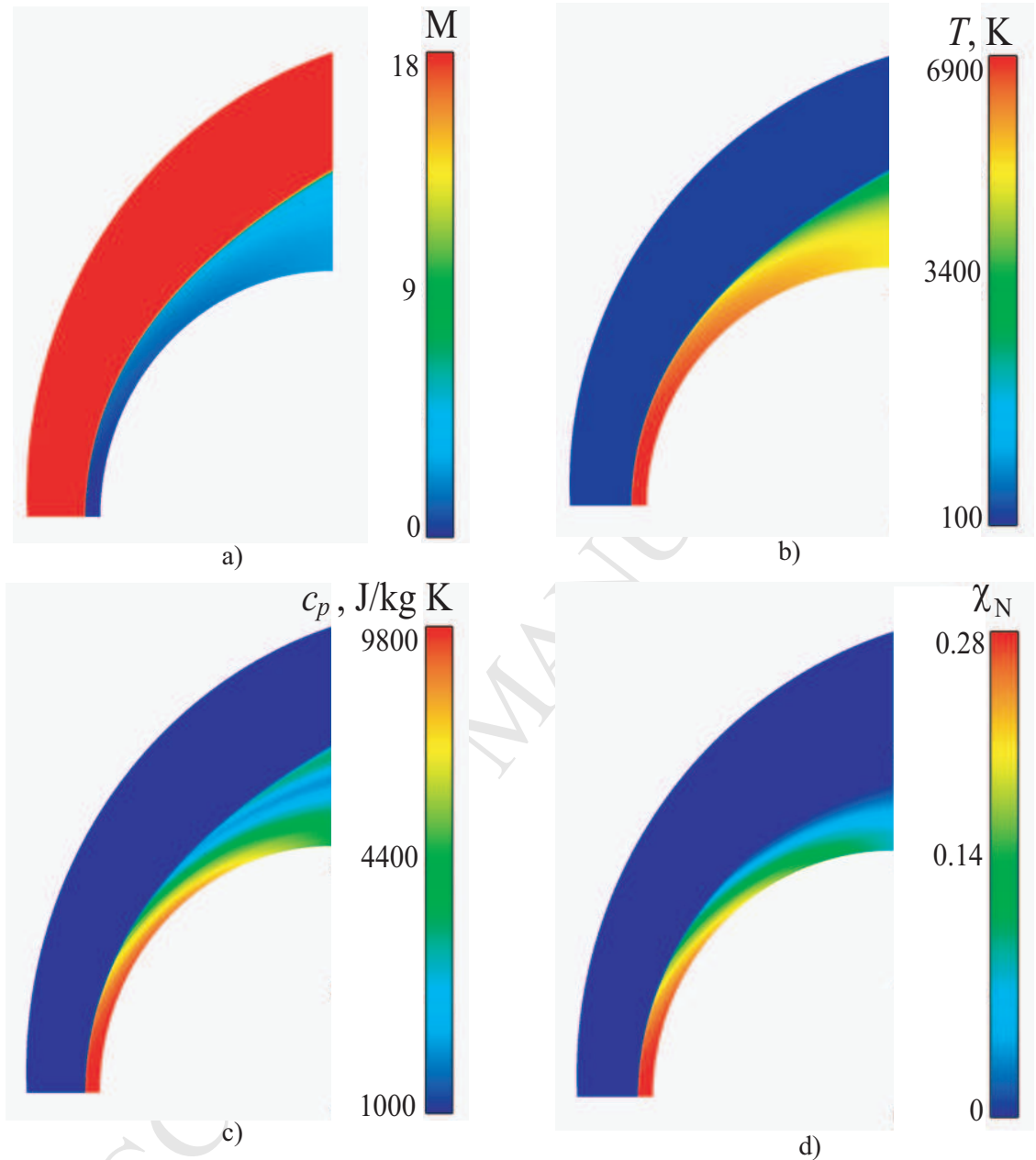
Figure 5. Contour plots of Mach number (a), temperatures (b), specific heat capacity at constant pressure (c) and mole fraction of atomic nitrogen (d) for M = 17.77

resulting in convective and radiative heat-flux.

The distributions of pressure, temperature and velocity along the stagnation line are shown in the Figure 6 (physical quantities are normalized on the free stream quantities). The lines 1 correspond to the model of perfect gas, and lines 2 correspond to the calculations with the model proposed in [30]. The ideal gas model overpredicts temperature in the shock layer because the internal energy is stored in the gas translational mode. The ideal gas model is a calorically perfect gas, and none of the other internal energy modes of the molecule are accounted for. Furthermore, the ideal N_2 remains as diatomic nitrogen and has not been allowed to dissociate which would otherwise absorb some of the internal energy as chemical energy. The temperature and non-dimensional pressure profiles along the stagnation line agree well with the axisymmetric solution presented in [36]. A small discrepancy is a consequence of the different treatment of physical quantities of equilibrium flow and the introduction of a more advanced upwind numerical scheme.
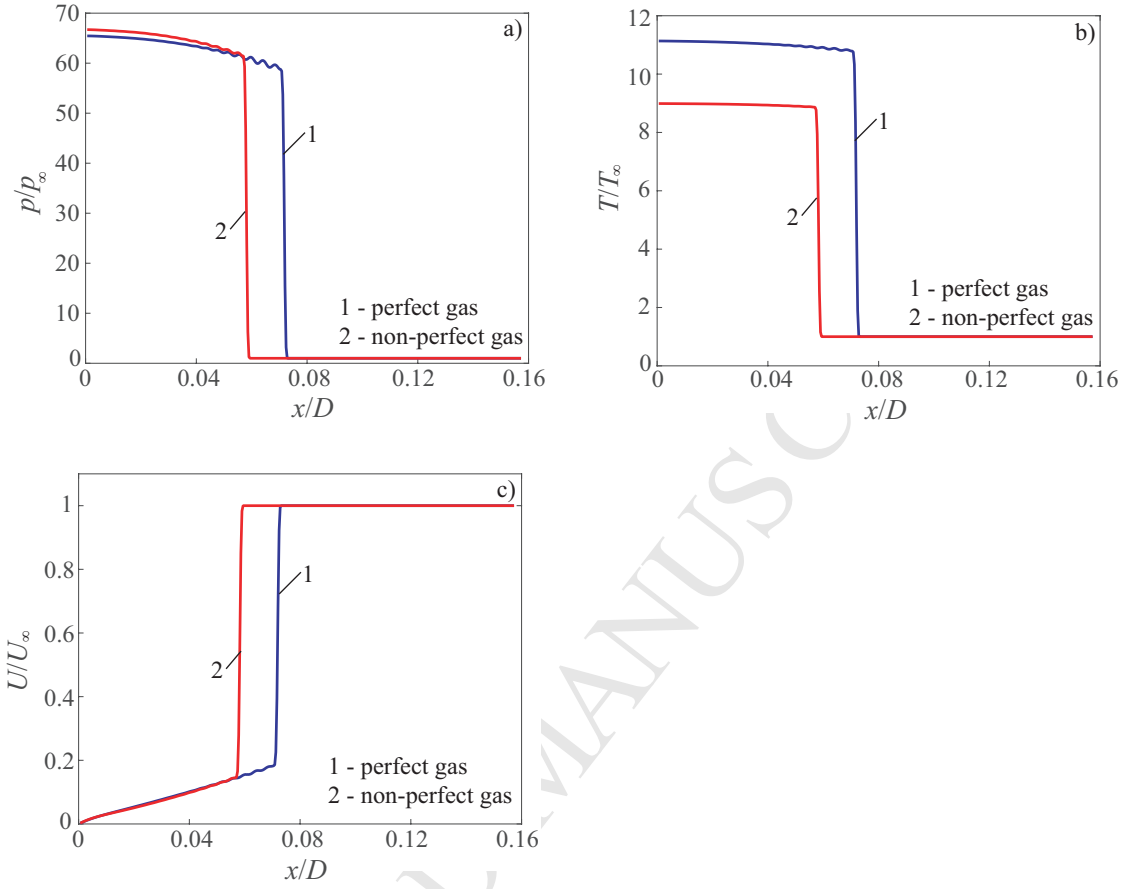
Figure 6. Distributions of pressure (a), temperature (b) and velocity (c) along the stagnation line for M = 7.106 (V = 2438.4 m/s)

Pressure distributions on sphere surface show Figure 7. The gas pressure behind the shock undergoes almost a homogeneous variation in the process of the increasing Mach number. But the increasing of temperature is slow initially and then becomes larger. The results are in a good agreement with those presented in [35].

Two important characteristics of the chemical equilibrium and perfect gas model distributions at the stagnation plane are concerned with the behind the shock flow variable magnitudes and the shock layer thickness. In comparison with the perfect gas model results, the results behind the shock wave obtained with the chemical equilibrium gas model are only slightly higher for pressure, considerably lower for temperature and higher for density. The higher density for the chemical equilibrium gas model leads to reduction of the shock standoff distance (shock layer thickness) in front of the sphere. The temperature, pressure and density behind the shock wave increase toward the sphere surface due to the continuous decrease in the flow velocity.

The density ratio has an important effect on the shock standoff distance in front of a sphere. An approximate expression for the shock standoff distance Δ on a sphere of diameter D is given by [31]

$$\frac{\Delta}{D} = K\varepsilon, \quad \varepsilon = \frac{\gamma - 1}{\gamma + 1}\left(1 + \frac{2}{\gamma - 1}\frac{1}{M_\infty^2}\right),$$

where ε is the density ratio across the shock on the stagnation streamline, and K is the correction factor (K = 0.39–0.41). For high velocities, density ratio becomes small compared to unity. Therefore, the density ratio across a normal shock wave has a major impact on
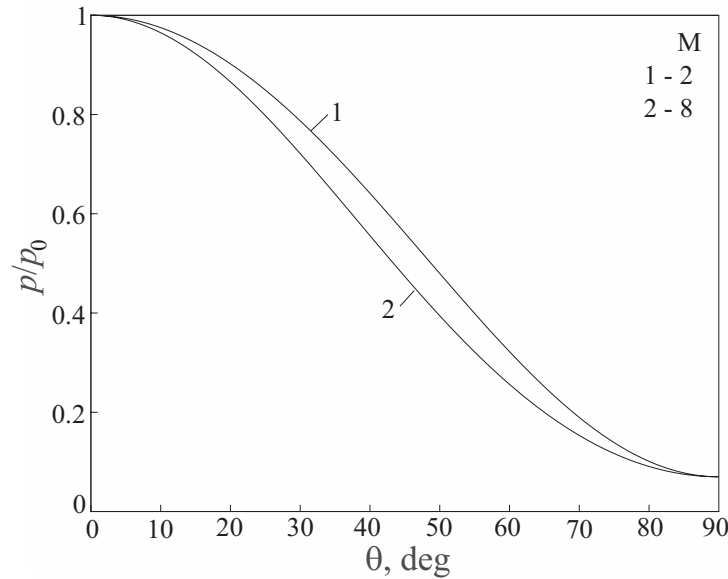
16

Figure 7. The ratio of the pressure at the sphere surface
and the pressure at the stagnation point behind a normal
shock wave for M = 2 (line 1) and M = 8 (line 2)

shock standoff distance. If the density ratio increases, then the shock standoff distance decreases. The chemical reactions increase the density ratio, which decreases the shock standoff distance. Therefore, in comparison to the calorically perfect gas results, the shock wave for a chemically reacting gas lies closer to the sphere (at the same velocity and altitude conditions).

Figure 8 shows that the shock standoff distance reduces with increasing free stream Mach number (increasing density behind the shock wave). Line 1 shows the shock standoff distance for air in full chemical equilibrium. Line 2 corresponds to the experimental measurements [31]. Line 3 gives the shock standoff distance for a perfect gas with $\gamma = 1.4$. The standoff distance decreases at first with the increasing Mach numbers, but it increases when Mach number becomes larger. The shock wave is closer to the wall for high Mach number. This is due to the fact that the temperature behind a shock wave increases with the Mach number increasing and goes up to induce the occurrence of chemical reactions for air components. Simultaneously, the pressure is also rising. However, the increase rates of the pressure and the temperature are not equal [3]. Since the calculated perfect gas normalized density values tend towards a finite maximum value of about 6 for air as the free stream Mach number increases, the shock wave thickness tends towards a minimum. For the Mach number about 10, the shock layer thickness is already close to this minimum since the normalized density is about 5.7. For the same free stream conditions, the chemical equilibrium gas shock layer is thinner than that for perfect gas and is continually changing with increasing free stream Mach number.

The shock standoff distance is directly proportional to the diameter of the sphere and inversely proportional to the density in the shock layer. For a perfect gas with $\gamma = 1.4$, the density ratio across the shock wave has a minimum value of 1/6. However, high velocity shock waves in air do not have such a limit, except at very low pressures where the relaxation times are large compared to the transit time for the air flowing over the sphere. The tendency is for the enthalpy to go into heat of formation in chemical reactions such as dissociation, rather than increasing the temperature of the air. The effect of dissociation is to increase the density and to decrease the shock detachment distance as compared to the perfect air
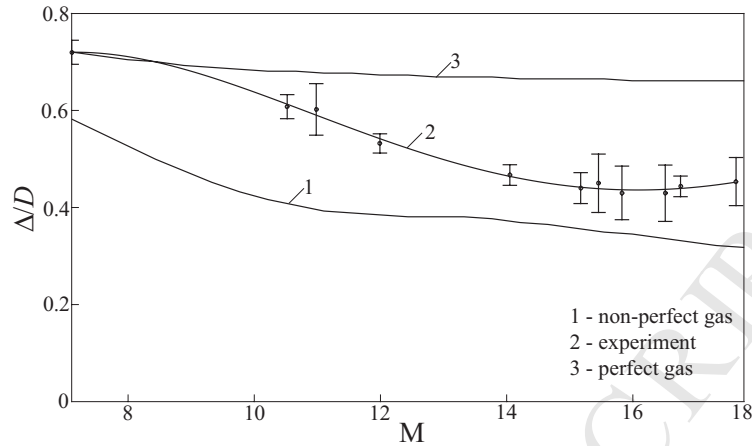
Figure 8. Dependence of the shock standoff distance on the free stream Mach number

result.

The shock standoff distance is smallest in the case of calorically perfect gas and the chemical non-equilibrium flow shock stand-off distance lies between calorically perfect gas and thermochemical equilibrium flow. In the case of calorically perfect gas, the kinetic energy of the flow ahead of the shock is mostly converted to translational and rotational molecular energy behind the shock. On the other hand, for a gas in thermal equilibrium or chemically reacting gas, the kinetic energy of the flow, when converted across the shock wave, is shared across all molecular modes of energy, and goes into the dissociation energy of the products of the chemical reactions. Hence, the temperature which is a measure of translational energy only, is less for such a case. In contrast, the pressure ratio is affected only by a small amount since pressure is a mechanically oriented variable and it is governed mainly by the fluid mechanics of the flow and not so much by the thermodynamics. The combined effect of pressure and temperature yields the density ratio across the shock which is more pronounced in case of a gas with internal energy excitation or chemically reacting gas. The shock standoff distance, which depends on the density ratio across the shock, therefore in this case is less as for non-reacting gas.

The computed drag coefficients for spheres are plotted in the Figure 9 against Mach number. Line 1 corresponds to the model of high-temperature air, and line 2 corresponds to the case of a perfect gas. Bullets shows measured drag coefficient from the ballistic range measurements [34]. The large drag rises in the subsonic regime associated with the drag-divergence phenomena and the decrease in drag in the supersonic regime. Drag approaches a plateau and becomes relatively independent of Mach number as Mach number becomes large. For a range of Mach numbers from 4 to 10, the drag coefficient is relatively constant at a value of 0.92.

Table 2 shows the execution time for various thermodynamic air models. Time discretization is based on the third-order Runge–Kutta scheme. Flux on the faces of the control volume are calculated with Godunov and Rusanov schemes. A perfect gas model and Kraiko model proposed in [30] are used as thermodynamic model of air.

Table 2. Computational time and speedup for hypersonic sphere problem. Different thermodynamic models and computational options
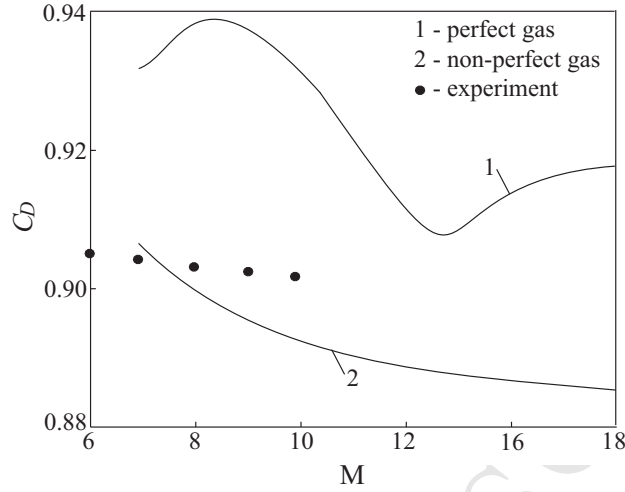
Figure 9. Dependence of the drag coefficient on
Mach number

Air model	Solver type	Server 1			Server 2		
		CPU	GPU	Speedup	CPU	GPU	Speedup
Perfect gas	Godunov	2.32	0.117	19.86	4.05	0.029	139.66
	Rusanov	1.78	0.106	16.79	2.85	0.027	105.41
Kraiko model	Godunov	45.96	0.242	189.91	84.08	0.061	1378.33
	Rusanov	45.42	0.232	195.76	81.94	0.058	1412.78

5.2 Hypersonic aircraft problem

In many hypersonic vehicles, the propulsion mechanism is integrated with the airframe [3]. In the integrated airframe propulsion concept for a hypersonic vehicle, the entire under surface of the vehicle is a part of the scramjet engine. Initial compression of the air takes place in the bow shock from the nose of the vehicle. Further compression and supersonic combustion occur inside a series of modules near the rear of the vehicle. The expansion of the combustion products is partially realized through nozzles in the engine modules and mainly over the bottom rear surface of the vehicle. The lift is produced by high pressure behind the bow shock wave and exerted on the relatively flat under surface of the vehicle. Integration of airframe and propulsion system makes the modelling and control of hypersonic vehicles challenging. As temperature rises because of compression and viscous effects, translational and vibrational motion of the fluid molecules are high enough to cause dissociation. Monitoring the dissociation of molecular oxygen molecules is most important as scramjets use molecular oxygen for the combustion oxidizer. If dissociation occurs, combustion process is limited in terms of available energy for the production of thrust. Hypersonic inlets must be appropriately modelled to determine chemical composition and the physical state of the air entering the combustion chamber.

The flow past of a hypersonic aircraft at zero angle of attack is considered. The model, shown in the Figure 10, approximately corresponds to NASA hypersonic aircraft X-43 presented in [4, 5, 9]. Full geometrical dimensions are unknown, and geometrical model is designed using some dimensions given in [4, 37]. The upper body of the vehicle is simply a flat surface, which is kept at zero angle of attack for simplicity. The lower surface consists of a frontal wedged surface, a scramjet engine with a constant cross sectional area and another trailing wedged surface. The frontal wedged surface serves as a diffuser for the flow entering

the scramjet, and the trailing surface acts as a propulsive surface. The aircraft three views and main dimensions are shown in the Figure 11 (dimensions are given in millimeters). The leading edge angle is 5°, the length of the engine 0.68 m, and the engine cross-section area is 0.3 m (height) by 0.5 m (span). The frontal area of the model is about 0.153 m². The flight conditions correspond to the Mach number M = 10 at an altitude of 30 km (the flight speed is $V = 2976.62$ m/s). At the given altitude, the atmospheric pressure and temperature are $p = 1172$ Pa and $T = 227$ K, respectively (density is 0.0184 kg/m³ and dynamic viscosity is 0.148×10^{-4} Pa·s). The results of wind tunnel tests are published in [37].
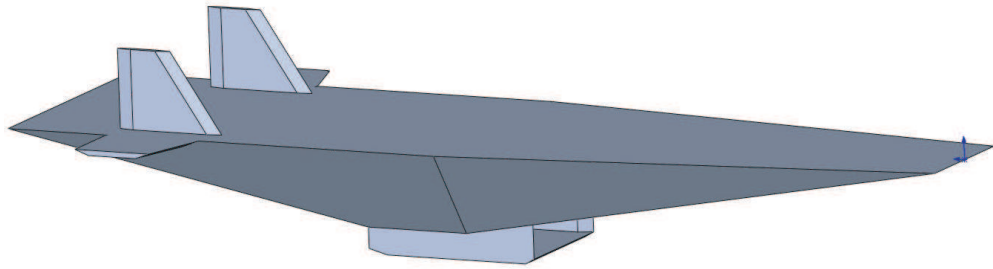

Figure 10. Model of hypersonic aircraft

The problem is solved in a three-dimensional formulation for half of the computational domain whose dimensions are chosen equal to $6 \times 4 \times 2$ m³. At the inlet boundary, the supersonic inflow conditions are specified, and supersonic outflow conditions are applied to outlet boundary. Slip and no-penetration boundary conditions are used on the walls. The surface of the body is assumed to be adiabatic. The mesh consists of 16 million cells and 48 million faces. The mesh contains 439221 boundary faces.

The distributions of the velocity magnitude, temperature, molar concentration of nitrogen oxide and effective heat capacity ratio in the plane of symmetry are shown in the Figure 12. Due to the fact that the aircraft has well streamlined shape, the gas temperature does not increase too much and relatively little nitrogen oxide is formed, while other components are practically not formed. Mole fractions of molecular oxygen and nitrogen oxide decrease as temperature past the shock wave increases. Therefore, the mole fraction of atomic nitrogen increases.

The temperature distribution on the aircraft surface is shown in the Figure 13. Level lines of the density gradient are shown in the cutting planes. The highest temperature is observed at the inlet to the air intake. The oblique shock wave created at the nose of aircraft propagates downstream underneath the vehicle and can impinge on the leading edge of the cowl of the scramjet engine. The inlet cowl has a blunt leading edge to reduce aerodynamic heating, and therefore a detached curved shock wave exists just upstream of the cowl leading edge similar to the blunt body flows. The shock from the nose of the vehicle does not impinge directly on the surface of the cowl, but rather on the cowl shock wave, setting up a rather complex shock-shock interaction that can change the nature of both shocks and the surrounding flow field. The observed shock wave structures are in a good agreement with the literature data [38, 39].

Pressure distributions and limiting streamlines on the aircraft surface are presented in the Figure 14. Limiting streamlines show location of vortex structures

Drag and lift coefficients as functions of angle of attack are shown in the Figure 15. The angle of attack varies from -10 to $+10$ degrees. In the range from 0 to 10 degrees, increase in angle of attack leads to increase in aerodynamic quality (ratio of lift and drag). Quantitative comparison with experimental data is difficult due to different shapes of hypersonic aircrafts, different flow regimes and reference parameters. However, qualitative dependencies of drag
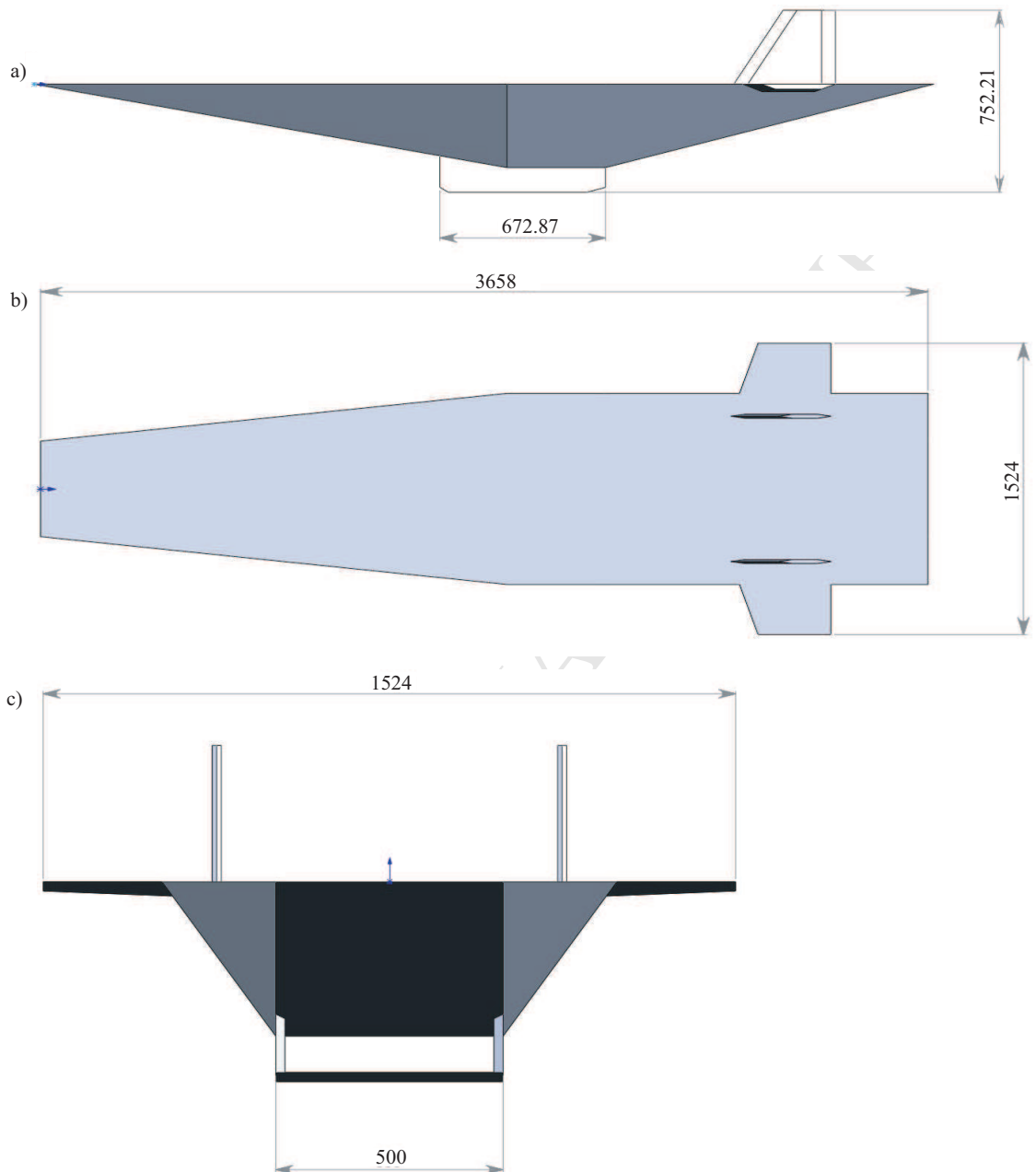
Figure 11. Three views of the hypersonic vehicle

and lift coefficients on angle of attack are similar to those observed experimentally. Dependance of drag coefficient is close to parabolic dependance, and dependance of lift coefficient is close to linear dependance.

To evaluate performance of the computational procedure, the model of perfect air without chemical reactions is implemented. Table 3 shows the execution time of one step with averaging over 10 iterations for various thermodynamic air models. Time discretization is based on the third-order Runge–Kutta scheme. Flux on the faces of the control volume are calculated with Godunov scheme. A perfect gas model and Kraiko model proposed in [30] are used as thermodynamic model of air. CPU code is not organized optimally with the Godunov scheme. Using GPU allows to get a significant acceleration compared to a single CPU core. The use of GPU leads to 10 times faster calculations compared to the calculations on CPU.
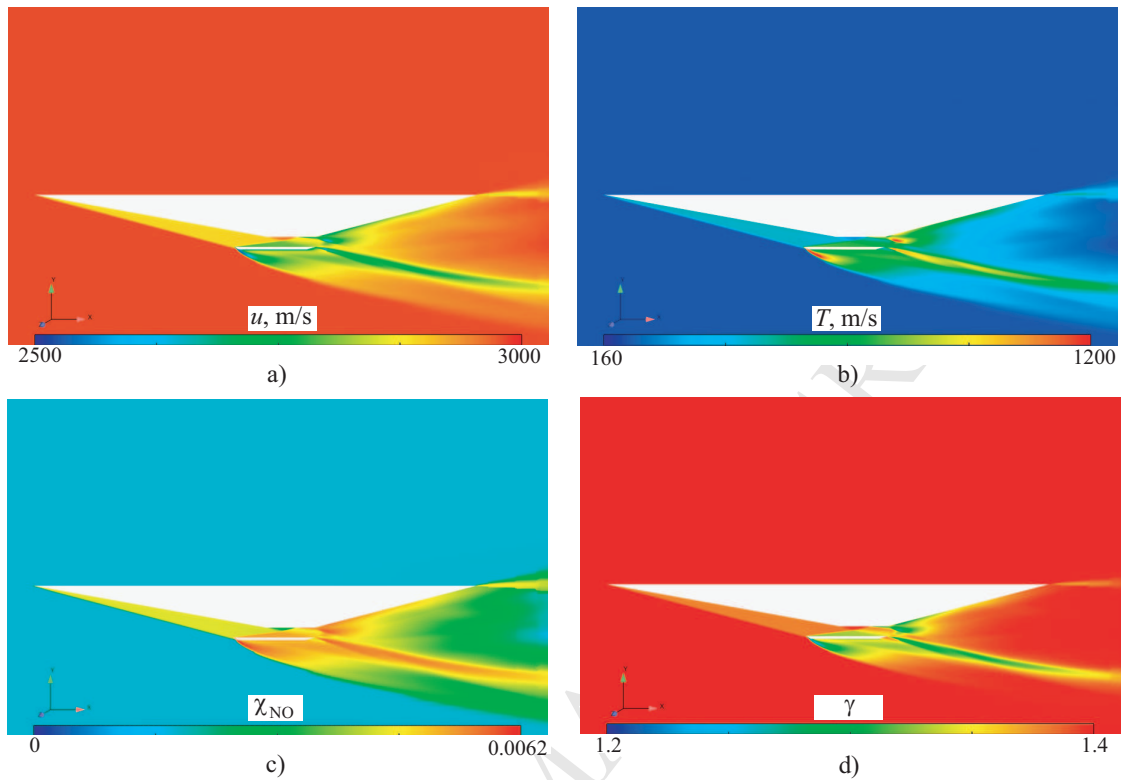
Figure 12. Contours of velocity magnitude (a), temperature (b), molar fraction of oxide nitrogen (c) and effective ratio of specific heat capacities (d) in symmetry plane
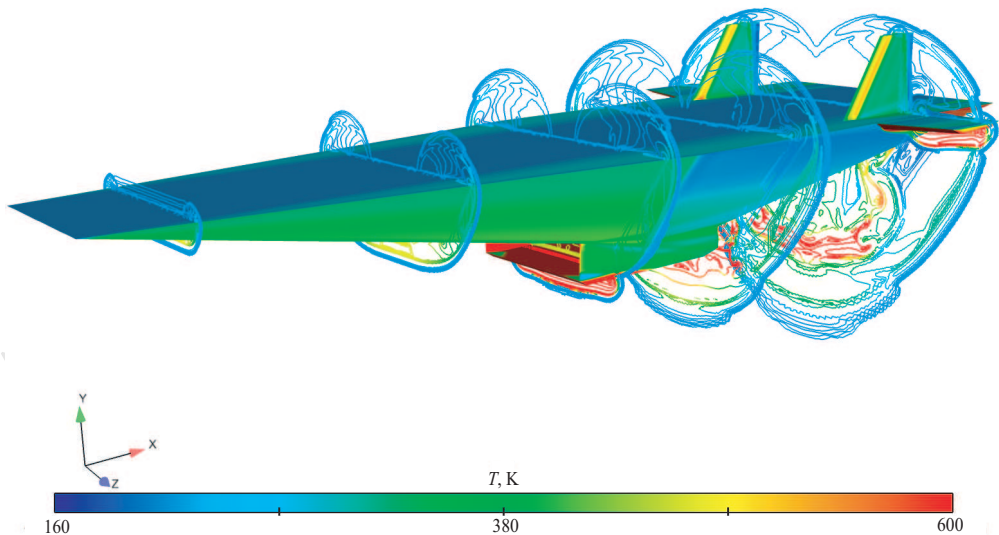

Figure 13. Contours of temperature and density gradient

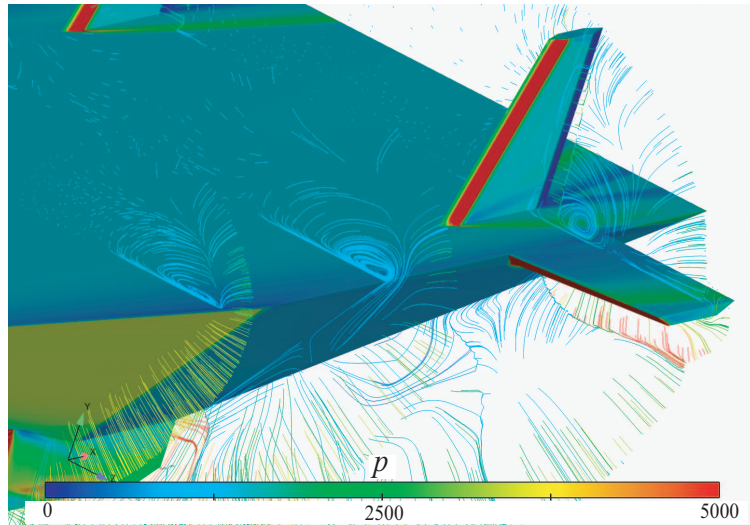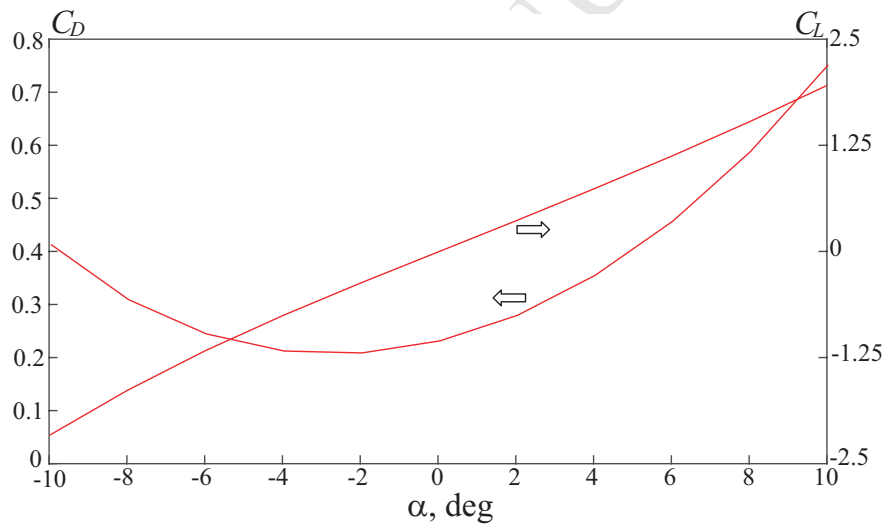| Air model	Server 1			Server 2		
	CPU	GPU	Speedup	CPU	GPU	Speedup
Perfect gas	134.40	8.61	15.61	212.42	1.80	117.81
Kraiko model	5009.49	19.76	253.47	3695.56	4.01	922.74

Figure 14. Contours of pressure and limiting streamlines

Figure 15. Drag and lift as functions of angle of attack for M = 6

6 Conclusion

The flowfield around a vehicle that flies at hypersonic speeds is one in which high-temperature gas effects strongly influence the forces acting on the surface (the pressure and the skin friction) and the heat transfer. Accurate prediction of these effects is critical to the design ensuring flight safety of any vehicle that flies at hypersonic velocities.

The finite volume method was applied to solve full Navier–Stokes equations on unstructured meshes, and CUDA technology was used for programming implementation of parallel computational algorithms. The developed CFD code is able to simulate hypersonic flows with a reasonable degree of confidence. The numerical results show that the high-temperature gas effects significantly change flowfield including the standoff distance of bow shock over the front part of sphere and other flow properties. The ability of the computations to accurately capture the shock shapes and the standoff distances demonstrates the capability of the code to model flows with high-temperature gas effects.

GPUs have evolved as a new paradigm for scientific computations. Cost/performance ratio and low power consumption make GPUs attractive for high-resolution CFD computations. However, in order to exploit the inherent architecture of the device, the numerical

Table 3. Computational time and speedup for hypersonic aircraft problem. Different thermodynamic models

algorithm as well as data structures are carefully tailored to minimize the memory access and any recursive relations in the computational algorithm. Speedup of solution on GPU with respect to solution on CPU is compared with the use of various meshes and computational options. Performance measurements show that numerical schemes developed achieve 20 to 50 speedup on GPU hardware compared to CPU reference implementation. The results obtained provide promising perspective for designing a GPU-based software framework for applications in CFD.

Acknowledgements

References

[1] Smirnov N.N. Ensuring safety of space flights. Acta Astronautica. 2017. Vol. 135. P. 1–5.

[2] Silnikov M.V., Guk I.V., Nechunaev A.F., Smirnov N.N. Numerical simulation of hypervelocity impact problem for spacecraft shielding elements. Acta Astronautica. 2018. Vol. 150. P. 56–62.

[3] Anderson J.D. Hypersonic and high temperature gas dynamics. AIAA, 2006. 811 p.

[4] Huebner L.D., Rock K.E., Ruf E.G., Witte D.W., Andrews E.H. Hyper-X flight engine ground testing for flight risk reduction. Journal of Spacecraft and Rockets, 2001, 38(6), 844–852.

[5] Reubush D.E., Nguyen L.T., Rausch V.L. Review of X-43A return to flight activities and current status. AIAA Paper, 2003, 2003-7085 (12 pages).

[6] Borovoi V.Ya., Skuratov A.S., Surzhikov S.T. Study of convective heating of segmental-conical martian descent vehicle in shock wind tunnel. AIAA Paper, 2004, 2004-2634 (11 pages).

[7] Deiwert G., Strawa A., Sharma S., Park C. Experimental program for real gas flow code validation at NASA Ames Research Centre. Washington: NASA, 1989.

[8] Wang Z., Sun X., Huang W., Li S., Yan L. Experimental investigation on drag and heat flux reduction in supersonic/hypersonic flows: a survey. Acta Astronautica, 2016, 129, 95–110.

[9] Mirmirani M., Wu C., Clark A., Choi S., Fidan B. Airbreathing hypersonic flight vehicle modeling and control, review, challenges, and a CFD-based example. Proceeding of the Workshop on Modeling and Control of Complex Systems, 30 June — 1 July 2005, Ayia Napa, Cyprus (15 pages).

[10] Yoon S., Gnoffo P.A., White J.A., Thomas J.L. Computational challenges in hypersonic flow simulations. AIAA Paper, 2007, 2007-4265 (16 pages).

[11] Schmisseur J.D. Hypersonics into the 21st century: a perspective on AFOSR-sponsored research in aerothermodynamics. Progress in Aerospace Sciences, 2015, 72, 3–16.

[12] Stalker R. Hypervelocity aerodynamics with chemical nonequilibrium. Annual Review of Fluid Mechanics, 1989, 21, 37–60.

[13] Tirsky G. Up-to-date gasdynamic models of hypersonic aerodynamics and heat transfer with real gas properties. Annual Review of Fluid Mechanics, 1993, 25, 151–181.

[14] Hilsenrath J., Klein M. Tables of thermodynamic properties of air in chemical equilibrium including second virial corrections from 1500 to 15,000 K. Tullahoma: Arnold Engineering Development Center, 1965. AEDC-TR-65-68.

[15] Bertin J., Cummings R. Critical hypersonic aerothermodynamic phenomena. Annual Review of Fluid Mechanics, 2006, 38, 129–157.

[16] Coblish J., Smith M., Hand T., Candler G., Nompelis I. Double-cone experiment and numerical analysis at AEDC Hyper-velocity wind tunnel No 9. AIAA Paper, 2005, 2005-0902 (12 pages).

[17] Tissera S., Titarev V., Drikakis D. Chemically reacting flows around a double cone, including ablation effects. AIAA Paper, 2010, 2010-1285 (16 pages).

[18] Chanetz B. Low and high enthalpy shock-wave/boundary layer interactions around cylinder-flare models. Progress in Flight Physics, 2012, 3, 107–118.

[19] Candler G.V., Nompelis I. CFD validation for hypersonic flight: real gas flows. NATO Report, 2002, RTO-TR-AVT-007-V3.

[20] MacCormack R.W. Carbuncle computational fluid dynamics problem for blunt-body flows. Journal of Aerospace Information Systems, 2013, 10(5), 229–239.

[21] Menne S., Weiland C., D'Ambrosio D., Pandolfi M. Comparison of real gas simulations using different numerical methods. Computers and Fluids, 1995, 24(3), 189–208.

[22] Boulahia A., Abboudi S., Belkhiri M. Simulation of viscous and reactive hypersonic flows behaviour in a shock tube facility: TVD schemes and flux limiters application. Journal of Applied Fluid Mechanics, 2014, 7(2), 315–328.

[23] Lockwood B., Mavriplis D. Gradient-based methods for uncertainty quantification in hypersonic flows. Computers and Fluids, 2013, 85, 27–38.

[24] Tchuen G., Burtschell Y., Zeitoun D.E. Computation of non-equilibrium hypersonic flow with artificially upstream flux vector splitting (AUFS) schemes. International Journal of Computational Fluid Dynamics. 2008. Vol. 22. No. 4. P. 1061–8562.

[25] Chen S., Hu Y., Sun Q. Study of the coupling between real gas effects and rarefied effects on hypersonic aerodynamics. AIP Conference Proceedings, 2012, 1501, 1515–1521.

[26] Chinnappan A.K., Malaikannan G., Kumar G. Insights into flow and heat transfer aspects of hypersonic rarefied flow over a blunt body with aerospike using direct simulation Monte-Carlo approach. Aerospace Science and Technology, 2017, 66, 119–128.

[27] Emelyanov V.N., Karpenko A.G., Kozelkov A.S., Teterina I.V., Volkov K.N., Yalozo A.V. Analysis of impact of general-purpose graphics processor units in supersonic flow modelling. Acta Astronautica, 2017, 135, 198–207.

[28] Gupta R.N., Scott C.D., Moss J.N. Slip-boundary equations for multicomponent nonequilibrium airflow. NASA Technical Report, 1985, TP-1985-2452.

[29] Lofthouse A.J., Scalabrin L.C., Boyd I.D. Velocity slip and temperature jump in hypersonic aerothermodynamics. Journal of Thermophysics and Heat Transfer, 2008, 22(1), 38–49.

[30] Kraiko A.N., Makarov V.E. Explicit analytic formulas defining the equilibrium composition and thermodynamic functions of air for temperatures from 200 to 20000 K. High Temperature, 1996, 34(2), 202–213.

[31] Lobb R.K. Experimental measurement of shock detachment distance on spheres fired in air at hypervelocities / High Temperature Aspects of Hypersonic Flow. Oxford: Pergamon Press, 1964, 519–527.

[32] McIntyre T.J., Bishop A.I., Rubinsztein-Dunlop H., Gnoffo P. Comparison of experimental and numerical studies of ionizing flow over a cylinder. AIAA Journal, 2003, 41(11), 2157–2161.

[33] Olivier H. A Theoretical model for the shock stand-off distance in frozen and equilibrium flows. Journal of Fluid Mechanics, 2000, 413, 345–353.

[34] Cox R.N., Crabtree L.F. Elements of hypersonic aerodynamics. New York: Academic Press, 1965.

[35] Holt M., Hoffman G.H. Calculation of hypersonic flow past sphere and ellipsoids. American Rocket Society, 1961, 61-209-1903.

[36] Olsen M.E., Liu Y., Vinokur M., Olsen T. Implementation of premixed equilibrium chemistry capability in OVERFLOW. AIAA Paper, 2004, 2004-1273.

[37] Engelund W., Holland S., Cockrell C., Bittner R. Propulsion system airframe integration issues and aerodynamic database development for the Hyper-X flight research vehicle. Proceedings of the 14th International Symposium on Air-breathing Engines, 5–10 September 1999, Florence, Italy. ISABE 99-7215.

[38] Silnikov M.V., Chernyshov M.V. The interaction of Prandtl–Meyer wave and quasi-one-dimensional flow region. Acta Astronautica, 2015, 109, 248–253.

[39] Silnikov M.V., Chernyshov M.V. Incident shock strength evolution in overexpanded jet flow out of rocket nozzle. Acta Astronautica, 2017, 135, 172–180.

Simulation of hypersonic flows with equilibrium chemical reactions on graphics processor units

V.N. Emelyanov[1], A.G. Karpenko[2], K.N. Volkov[3]

[1]Baltic State Technical University, St Petersburg, Russia
[2]St Petersburg State University, St Petersburg, Russia
[3]Kingston University, London, United Kingdom

- Simulation of hypersonic flow with equilibrium chemical reactions is performed
- The results are in agreement with experimental and computational data
- High-temperature gas effects change flowfield around hypersonic aircraft
- Possibilities of the use of graphics processor units for are demonstrated